J. Fluid Mech. (2008), vol. 616, pp. 135–152. © 2008 Cambridge University Press
doi:10.1017/S0022112008003650 Printed in the United Kingdom

Experimental observation of swirl accumulation in a magnetically driven flow

I. GRANTS, C. ZHANG, S. ECKERT AND G. GERBETH

Forschungszentrum Dresden–Rossendorf, PO Box 510119, 01314 Dresden, Germany
i.grants@fzd.de

(Received 29 February 2008 and in revised form 7 August 2008)

Independent poloidal and azimuthal body forces are induced in a liquid metal cylinder by travelling and rotating magnetic fields of di erent frequencies, respectively. The bulk axial and azimuthal velocities are measured by the ultrasound Doppler method. Particle image velocimetry is used to observe the upper free surface velocity distribution. The transition from the poloidal to the azimuthal body force governed regime occurs at a fixed ratio of the respective force magnitude of around 100. This transition is marked by the formation of a concentrated vortex revealing several similarities to intense atmospheric vortices. The vortex structure is controlled by a relatively weak azimuthal force while the maximum speed of the swirl is mainly governed by the poloidal one. Under a certain force ratio the average axial velocity changes its direction in the vortex core, resembling the subsidence in an eye of a tropical cyclone or a large tornado. Multiple moving vortices encircle the vortex core in this regime.

1. Introduction

Angular momentum conservation leads to a swirl enhancement towards the centre of a converging flow. This phenomenon, also known as vortex stretching, is observed in di erent spectacular flows ranging from the bathtub vortex (Shapiro 1962; Andersen et al. 2006) to tornados (Klemp 1987) to tropical cyclones (Emanuel 1991, 2003). Atmospheric vortices are usually simulated in open flows where the fluid continuously leaves and re-enters the working volume (Ward 1972; Montgomery, Vladimirov & Denissenko 2002). The related bathtub vortex also occurs above a sink where the fluid leaves the volume. The tornado-like vortices in laboratory are, thus, often implicitly associated with mass removal of fluid. The latter occurs in nature due to condensation of water vapour in tornado or hurricane clouds. The mass removal is not, however, a prerequisite as evidenced by the existence of so-called dust devils (Maxworthy 1973). Nonetheless, laboratory observations of swirl accumulation in body-force-driven enclosed flows are few. A controversial laboratory manifestation of the phenomenon concerns the flow driven by a primarily poloidal body force due to an electric current injected through a small electrode in a hemisphere of liquid metal (Sozou & Pickering 1976). Depending on the direction of current injection the principal body force points towards or away from the central electrode (Bojarevics & Scherbinin 1983; Bojarevics et al. 1989). When the flow converges towards the electrode, an intense swirl is observed experimentally provided that the current is large enough. The opposite current however large causes no swirl at the surface. Bojarevics & Scherbinin (1983) explained the observations in terms of a similarity solution in a semi-infinite layer emerging above a certain critical value of the poloidal force strength. This similarity solution has the form of a concentrated vortex gaining

angular momentum from the far field. A shortcoming of the experiment was the lack of any control over the angular momentum source which was evidently present (see discussion by Davidson et al. 1999; Davidson 2001). A shortcoming of interpretation, in turn, is an impression it may leave that a continuous external supply of angular momentum is not needed to support a persistent swirl in a finite volume. Concerned by this fact, Davidson et al. (1999) disputed whether the observed rotation had anything at all to do with a concentrated vortex. They proposed an alternative explanation of 'poloidal suppression'. This means that there is no vortex accumulation and the meridional flow is suppressed by uniform (almost rigid-body) rotation due to a relatively weak uncontrolled source of angular momentum. Instead of the singular point electrode force, they considered theoretically and numerically the flow caused by smooth poloidal and azimuthal body forces. Their study was focused on a regime where a uniform rotation due to an apparently negligible azimuthal force dominates the flow and suppresses the poloidal motion. They showed that such a regime may set in at a strikingly low azimuthal force of about just a few per cent of the poloidal one. A small azimuthal force being imposed by an outer current loop field and/or the magnetic field of the Earth in the experiment by Bojarevics & Scherbinin (1983) may have been su cient to provide the dominance of the swirl. Nevertheless, they also admitted a possibility of another flow regime with loosely specified properties referred to as 'di usive structure' when the source of angular momentum is yet weaker. We shall see that this 'di usive structure' is nothing else than a concentrated vortex sharing several generic properties of a tornado.

Our intention is to scan comprehensively the transition between the poloidal and azimuthal body force governed states in an enclosed flow in the search for a concentrated vortex. Instead of the electrode current, we apply a combination of travelling and rotating magnetic fields to a cylindrical volume of liquid metal. These magnetic fields introduce smooth body forces in the axial and azimuthal directions, respectively. Such a configuration enables a separate control of both body forces, which are independent of the flow. Our approach allows us to eliminate other factors that are often implicitly associated with a tornado-like vortex, namely, mass sink, concentrated forces as well as any feedback between the flow and its driving force. The aim of our study is to show the most persistent features of a concentrated vortex in a converging flow. For this purpose we compare the flow properties in our experiment with generic properties of intense atmospheric vortices or their laboratory models. Another aim is to quantify experimentally the ratio of poloidal and azimuthal driving forces required for the formation of a tornado-like vortex as well as to show the ability of a relatively weak distributed angular momentum source to prevent swirl accumulation. The latter may be regarded as an experimental verification of the theoretically anticipated 'poloidal suppression' (Davidson et al. 1999).

The phenomenon of swirl accumulation is potentially important in any converging flow. On the one hand, the properties of a concentrated vortex can be used in flow engineering. For example, the magnetic body-force-driven swirl concentration may assist entrapment of floating additives into the molten metal (see Gelfgat, Skopis & Grabis 2005). On the other hand, the appearance of a concentrated vortex may provide an insight into conditions of its formation.

2. *Magnetic body forces*

The travelling and rotating magnetic fields induce axial and azimuthal body forces, respectively, in a cylinder of liquid metal. Under low-frequency and low-induction

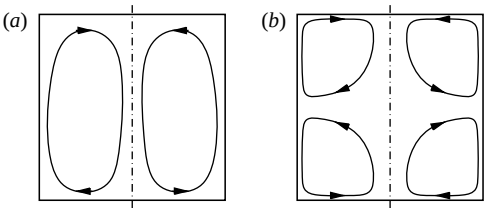

Figure 1. Schematic representation of the meridional flow topology in (a) an upward TMF and (b) an RMF.

conditions these body forces have simple expressions and do not depend on the flow. These conditions are commonly satisfied in a small-scale experiment like ours at frequencies in the range of 50 Hz. If, additionally, the wavelength of the travelling magnetic field (TMF) exceeds considerably the dimensions of the cylinder, then the average axial force is given by Grants & Gerbeth (2004) as

$$f_z = \tfrac{1}{4}\sigma\omega_T B_T^2 \kappa r^2, \tag{2.1}$$

where σ is the electric conductivity, κ is the axial wavenumber, ω_T is the angular frequency and B_T is the e ective value of the TMF induction. Note that the field amplitude is traditionally used in theoretical works. Here we report our results in terms of the e ective value which is the actually measured quantity. In the case of a rotating magnetic field (RMF) the expression for the average azimuthal force (Gorbachev, Nikitin & Ustinov 1974) is

$$f_\varphi = \sigma\omega_R B_R^2 r f(r,z), \tag{2.2}$$

where the subscript R refers to the RMF. The dimensionless shape function $f(r,z)$ has a maximum at mid-height of the cylinder and becomes zero at the horizontal electrically insulating endwalls.

When applied separately the TMF pulls the liquid metal with it along the sidewall. The flow returns through the central part where the axial body force is weaker (Grants & Gerbeth 2004; Lantzsch et al. 2007). There is a converging flow at one end of the cylinder as shown schematically in figure 1(a). A separately applied RMF drives a swirling flow which also causes a secondary meridional recirculation. The flow has an almost rigidly rotating core (Davidson 1992) within which the mean magnetic body force is balanced by the Coriolis force (product of radial and angular velocities). The source of meridional flow is the Ekman pumping due to the angular velocity gradient in the horizontal boundary layers. Thus, all streamlines of the meridional flow pass through these boundary layers forming two symmetric tori (figure 1b) in a closed cylinder.

The simultaneous application of RMF and TMF causes three-dimensional cross-term forces (Cramer, Pal & Gerbeth 2007) with frequencies $|\omega_R \pm \omega_T|$ besides (2.1) and (2.2). For $\omega_R = \omega_T$, there is a stationary three-dimensional force which breaks the rotational symmetry of the flow (Cramer et al. 2007). Therefore, we used considerably di erent frequencies $\omega_R \neq \omega_T$ making the cross-term forces rapidly oscillating and, thus, eliminating their net e ect on the flow. An axisymmetric flow driven by the combined fields has also been considered numerically (Gelfgat, Krūmiņš & Abricka 1999; Stiller et al. 2006) without a particular focus on the swirl accumulation phenomenon. Still, the results provide some indication of a concentrated vortex.

The dimensionless parameter of the magnetic source of azimuthal vorticity is the so-called forcing parameter (Grants & Gerbeth 2004)

$$F = \frac{\sigma \omega_T B_T^2 \kappa R^5}{2\rho\nu^2}, \tag{2.3}$$

where R is the radius of the cylinder and the magnetic Taylor number is the corresponding measure of the swirl source

$$\mathrm{Ta} = \frac{\sigma \omega_R B_R^2 R^4}{\rho\nu^2}, \tag{2.4}$$

where ν and ρ denote kinematic viscosity and density of the liquid metal, respectively. With characteristic values of these governing dimensionless parameters above 10^6 the flow was always turbulent in our experiments.

3. *Description of experiment*

3.1. Cell and surface conditions

The low-temperature alloy $Ga^{68}In^{20}Sn^{12}$ (melting point 10°C) was used with properties $\sigma = 3.2 \times 10^6\,\mathrm{S\,m^{-1}}$, $\rho = 6.36 \times 10^3\,\mathrm{kg\,m^{-3}}$ and $\nu = 3.4 \times 10^{-7}\,\mathrm{m^2\,s^{-1}}$. The melt was in a cylindrical Plexiglas container with an inner diameter $D = 2R$ equal to 90 mm and a wall thickness of 5 mm. The height of the liquid metal was 100 mm.

The melt surface was either covered by a thin (approximately 1 mm) layer of HCl solution or exposed to the air. In the latter case a thin film of solid oxidation products forms. Such a film imposes velocity boundary conditions close to no-slip. The acid layer dissolves the oxidation film and provides boundary conditions close to stress-free. Both conditions were used in combination with ultrasound Doppler velocimetry (UDV) and particle image velocimetry (PIV) on the surface, respectively. It is important for UDV to maintain a su cient amount of tracers in the bulk. The natural tracer particles are slowly dissolved in the presence of the acid layer, thus disabling continuous UDV measurements. For PIV, in turn, it is crucial to have a moving surface.

3.2. Magnetic fields

Two magnetic systems have been used in the experiments. Both of them allow independent control of B_T, B_R, ω_T and ω_R. The smaller system allows easier access to the bottom of the cell and, therefore, it is used for vertical velocity measurements. The larger one is used for azimuthal velocity measurements since it provides access from the side.

The smaller system is equipped with a ferromagnetic shell and has an inner bore diameter of 0.2 m and a height of 0.3 m. Six coils are arranged in one pole-pair connection to deliver an RMF with the maximum e ective magnetic induction of 12 mT. The TMF is generated by six coils at an equal distance of $h = 0.048$ m, which corresponds to a wavenumber $\kappa = 2\pi/6h = 21.8\,\mathrm{m^{-1}}$. The maximum TMF induction is 20 mT.

The larger system is free of ferromagnetic parts. Its bore is 0.365 m in diameter and 0.45 m in height. The TMF is generated by six coils at an equal distance of 0.075 m producing a wavenumber of $\kappa = 14\,\mathrm{m^{-1}}$. The maximum magnetic inductions for the RMF and TMF are 12 and 15 mT, respectively.

The RMF frequency is kept constant at 15 Hz. Di erent TMF frequencies of 50 and 75 Hz in the smaller and larger inductors, respectively, are used to compensate the wavelength di erence. The forcing parameter is, thus, $F \approx c_T B_T^2$ in both inductors, where $c_T = 2.6 \times 10^6\,\mathrm{mT^{-2}}$ is a constant. The magnetic Taylor number is $\mathrm{Ta} = c_R B_R^2$ with the constant $c_R = 1.7 \times 10^6\,\mathrm{mT^{-2}}$.

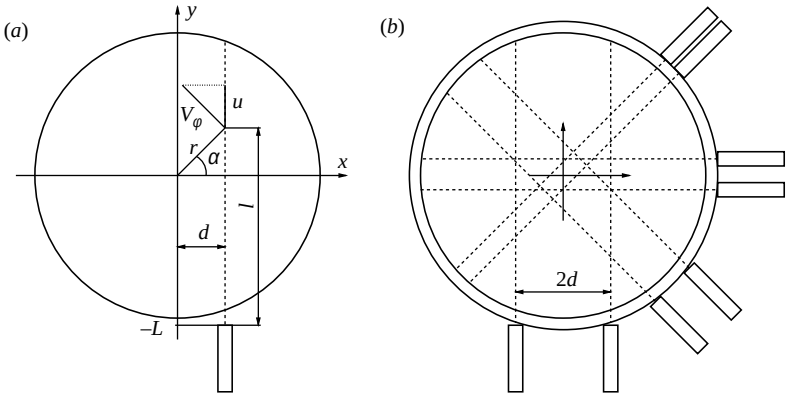

Figure 2. (a) Scheme of azimuthal velocity reconstruction and (b) probe placement for azimuthal velocity measurements ($2d$ = 12, 16, 20 and 30 mm).

The maximum shielding parameter is $\sigma \mu_o \omega_T R^2 \approx 4$ at 75 Hz where μ_o is the magnetic permeability of vacuum. Although the force distribution is already distorted by the skin e ect, the mean flow is little influenced at such a shielding (Lantzsch et al. 2007).

The container was placed at mid-height of the inductor. To ensure rotational symmetry of the axial force (2.1) the container was carefully centred with respect to the TMF coils. For this purpose the radial component of the TMF was measured at several places along the outer sidewall of the container. The position was adjusted to minimize the variation in these readings. All measurements were done for an upward TMF with the exception of a few explicitly specified cases of a downward TMF.

3.3. Ultrasound Doppler velocimetry

We measured the bulk flow by the ultrasound Doppler velocimeter DOP2000 (model 2125, Signal Processing SA) with 4 MHz (TR0405LS) and 8 MHz (TR0805LS) transducers. It is based on the pulse-echo technique and allows the measurement of the flow velocity projection on the ultrasound beam in real time (Takeda 1991; Cramer, Zhang & Eckert 2004). The measuring volumes can be considered as series of disks lined up along the beam centreline. The measuring volume size depends on several factors such as the transducer emitting frequency, the piezoelectric element diameter, the sound velocity in the liquid and the number of cycles composing the emitted bursts. Due to the divergence of the ultrasound beam, the lateral sizes of the measuring volume increase with the distance from the transducer. The standard 5 mm diameter 8 MHz transducer gives a spatial resolution of 0.69 mm in the axial direction and 7.1 mm in the lateral direction at a distance of 100 mm ahead of the transducer. Depending on di erent flow conditions, the sampling frequency of the velocity profiles can be adjusted by changing the pulse repetition frequency and emissions per profile. In the present experiments, we used various sampling frequencies ranging from about 5 to 50 Hz, depending on the velocity magnitudes to be measured. For the ultrasonic measurements there was no need to insert additional tracers into the melt as the number of naturally present particles (microbubbles, oxides) was su cient.

The measurement of the axial velocity profile is straightforward since it is equal to the velocity projection on a vertical beam. The azimuthal velocity can be directly measured only at a single point where the beam is parallel to the azimuthal direction. With some algebra a portion of the radial profile of the azimuthal velocity can be

reconstructed from measurements along a horizontal o -centre beam (see figure 2a). The radial and azimuthal velocities contribute to the UDV signal as

$$u = V_\varphi \cos(\alpha) + V_r \sin(\alpha). \tag{3.1}$$

Assuming axial symmetry of the time-averaged flow the contribution of radial velocity can be eliminated by averaging over $\pm\alpha$. This leads to

$$V_\varphi = \bar{u}/\cos(\alpha), \tag{3.2}$$

$$r = d/\cos(\alpha), \tag{3.3}$$

where $\alpha = \arctan[(l - L)/d]$ and $\bar{u} = [u(\alpha) + u(-\alpha)]/2$. † Evidently, the reconstruction is possible only when $r \gg d$. A smaller d, thus, enables a deeper view but also causes a larger error. For the purpose of cross-checking we installed eight sensors arranged in parallel pairs at an equal height as shown in figure 2(b). The measurements are done at mid-height of the container with a few explicitly stated exceptions. The approach theoretically also enables measurements of radial velocity profiles but practically this turned out impossible. The uncertainty of the actual beam coordinate strongly amplifies the measurement error by a $1/\sin(\alpha)$ factor for small α. At larger α, in turn, the result is biased by the non-symmetry due to the beam divergence.

3.4. Particle image velocimetry

The acid layer motion has been visualized by a digital video camera (Canon XL1) from above with the lens perpendicular to the surface. The acid layer is, thus, projected into a two-dimensional view. The camera delivers a series of consecutive snapshots with 720 × 576 pixel resolution at 25 frames per second, and the image window in the experiment was 100 mm × 80 mm. Minute particles with a diameter of 3 μm were added to the acid layer as tracers. The acquired pictures were analysed by the PIV program PIVview2C (PIVTEC Ltd., Göttingen).

There was no possibility for a laser sheet illumination due to the confinement by the magnetic systems, so we had to rely on the normal lamp light. The melt surface may produce strong reflections and so in that case the contrast is insu cient to apply PIV. To avoid this the camera distance and position were adjusted so that the reflection of the lens cap produced a dark background over most of the surface. A full coverage was, however, unachievable due to the deformation caused by surface tension at the periphery region close to the cylinder wall. This was a persistent source of spurious data there.

Two di erent shutter speeds of 1/50 and 1/250 s were used during the measurements. For PIV we used the higher shutter speed in order to avoid streak lines coming from the long exposure time. The picture series was analysed by a multi-grid interrogation method with an interrogation window of 24 × 24 pixels (50 % overlap). The velocity fields were obtained on a 59 × 47 grid, with a spatial resolution of 1.7 mm. They were finally median-filtered using a 3 × 3 kernel and smoothed by a Gaussian weighted kernel of one node width. The flow was also visualized by streak lines of moving tracers at a longer exposure of 1/50 s.

† The idea of separation of azimuthal and radial velocities in the UDV signal was suggested by an anonymous reviewer. Initially we assumed negligible contribution of the radial velocity which produced very similar results in the central part.

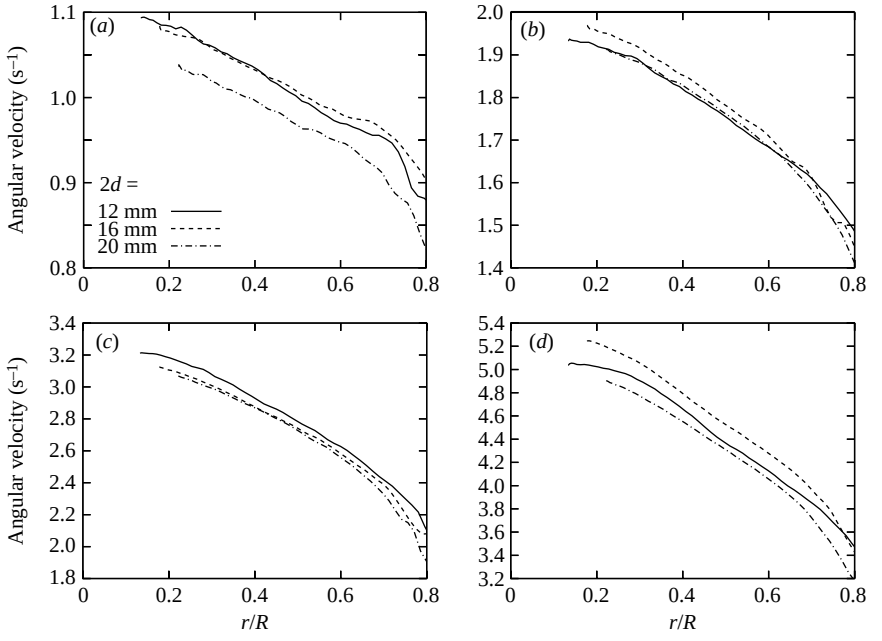

Figure 3. The time-averaged radial profiles of the angular velocity for pure RMF obtained by di erently displaced sensor pairs (see figure 2b). B_R = 0.54, 0.81, 1.08, 1.62 mT for (a–d), respectively.

4. Results

4.1. Bulk azimuthal velocity measurements

The reconstruction of mean azimuthal velocity profiles given by (3.2) relies on the assumption of axial symmetry of the flow. This condition is satisfied in RMF-alone-driven flow (B_T = 0) for which we obtained a good agreement between data sets obtained by di erent pairs of UDV sensors. Figure 3 shows the radial profiles of the mean angular velocity reconstructed by (3.2). Each of these profiles is an ensemble average of data from three to six runs. The standard deviation of separate components in each of these series was about 10 %. The agreement of the ensemble-averaged profiles from di erent sensor pairs was (somewhat unexpectedly) much better over a large portion of the beam line. The angular velocity slightly increased inwards. The characteristic di erence between the outer and the central parts varied between 15 and 40 % for B_R = 0.54 and 1.62 mT, respectively.

The agreement between di erent sensor pairs deteriorated gradually as the TMF strength was increased. Figure 4 shows the radial profiles of the reconstructed azimuthal velocity in the presence of TMF. A stronger deviation of the $2d$ = 30 mm sensor readings can be partly explained by a possible flow asymmetry which, as we shall see later, grows with the relative strength of TMF. Besides, the UDV beam may be refracting at the inclined container sidewall, thus e ectively reducing the value of d. The good agreement between all $2d$ □ 20 mm sensor readings shows that the possible e ect of beam refraction is negligible at these positions. All sensors confirmed an increase of the average azimuthal velocity in the presence of TMF. The latter observation is further quantified for di erent RMF flux densities in figure 5(a). This figure shows the velocity at the point where the beam is parallel to the azimuthal direction (y = 0). At this point the azimuthal velocity is equal to the velocity projection

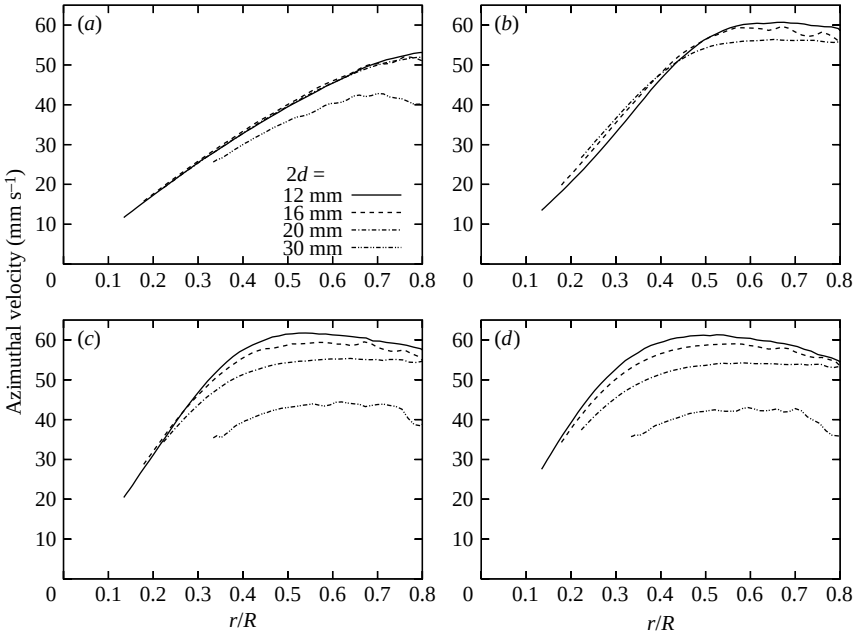

Figure 4. The time-averaged azimuthal velocity profiles for $B_R = 0.81$ mT and $F/\mathrm{Ta} = 0$, 31, 49, 97 for (a–d), respectively.

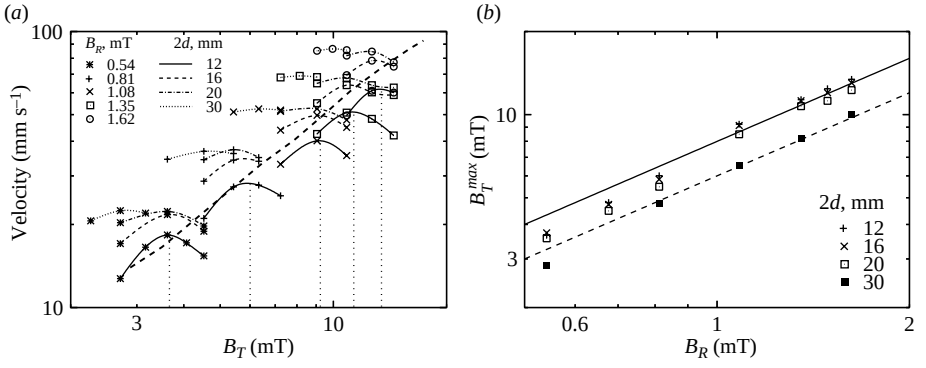

Figure 5. (a) The maximum azimuthal velocity versus TMF forcing. The maximum downward velocity on the axis for $B_R = 0$ is shown with a bold dashed line. (b) Conditions of maximum swirl concentration at various radial positions. The solid straight line and dashed straight line represent equations $F = 100\mathrm{Ta}$ and $F = 57\mathrm{Ta}$, respectively.

on the beam and, thus, the measurement is independent of the assumption behind the reconstruction given by (3.2). For each value of B_R a maximum of the time-averaged azimuthal velocity was observed at some TMF strength $B_T^{\max}$ which varied depending on the sensor displacement d. The vertical dotted lines in figure 5(a) mark these 'optimum' values for $2d = 12$ mm. Figure 5(b) shows the conditions of the maximum azimuthal velocity represented by $B_T^{\max}(B_R)$. This relation was well approximated by the equations $F/\mathrm{Ta} \approx 100$ for $2d \gtrsim 20$ mm or $F/\mathrm{Ta} \approx 57$ for $2d = 30$ mm.

So far the results concern velocities at the mid-plane. Figure 6 compares the e ect in terms of unprocessed velocity projection data at two additional heights 10 mm

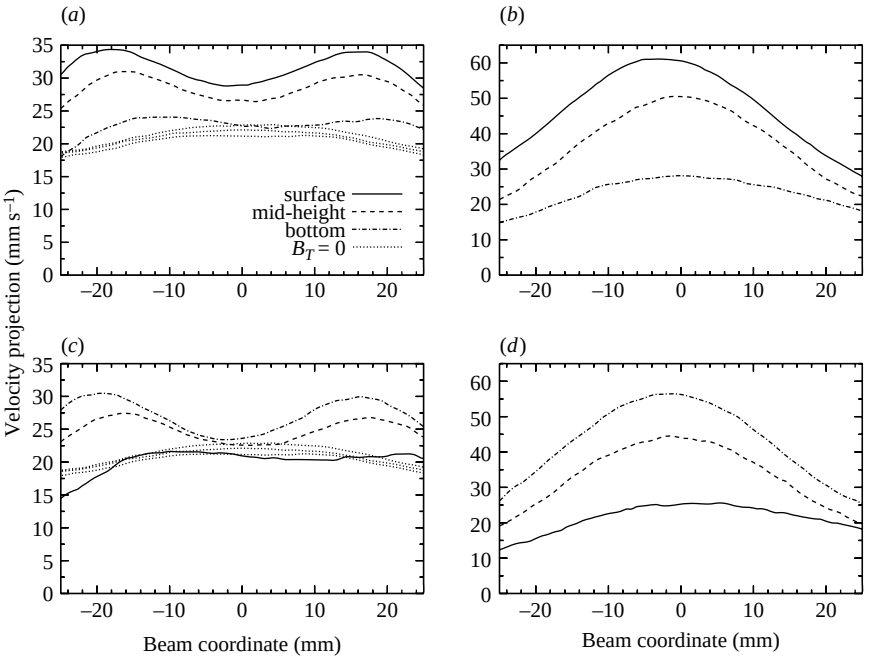

Figure 6. Time-averaged velocity projection versus beam coordinate for (a, b) upward and (c, d) downward TMF at various vertical positions; (a, c) $F/\mathrm{Ta} = 45$ and (b, d) $F/\mathrm{Ta} = 103$; the RMF flux density is fixed $B_R = 1.35\,\mathrm{mT}$ and the sensor displacement $2d = 12\,\mathrm{mm}$. The almost overlapping three dotted curves in (a, c) are for $B_T = 0$ at the same three di erent heights.

below the surface or above the bottom, respectively. The profiles were practically independent of the height for the case of a pure RMF-driven flow. The two values of TMF considered here correspond approximately to the maximum swirl enhancement at $2d = 30\,\mathrm{mm}$ and $2d \approx 20\,\mathrm{mm}$ (cf. figure 5). A considerable axial variation of profiles was observed at these values of TMF. The time-averaged velocity was most enhanced at that end of the liquid cylinder where the TMF-driven poloidal flow converged. At the opposite end there was almost no enhancement. Upon change of the TMF direction the top and bottom profiles exchanged symmetrically with little variation otherwise.

The axial velocity profile was marked by a slightly unsymmetric double torus structure in the RMF-alone-driven flow (short-dashed curve in figure 7a). The loss of vertical symmetry was most likely caused by imperfect surface boundary conditions which may depart from the no-slip due to some motion of the thin oxide film. The axial velocity was weak in comparison to the swirl (cf. figure 3d) in accordance with the 'poloidal suppression' (Davidson et al. 1999). The vertical upward velocity grew in the lower cell which gradually extended over the entire height as the TMF was increased. The maximum upward velocity at the centreline was reached at a certain $B_T = B_T^{rev}$, which was about 10.6 mT for the particular case shown in figure 7(a). Figure 7(b) displays the dependency $B_T^{rev}(B_R)$ and compares it to the condition of maximum swirl concentration observed by the sensor pair with $2d = 30\,\mathrm{mm}$. The upward flow direction on the axis contradicts common sense suggesting a downward return flow in the centre. The condition of a maximum of the upward velocity coincided approximately with the condition of the azimuthal velocity maximum

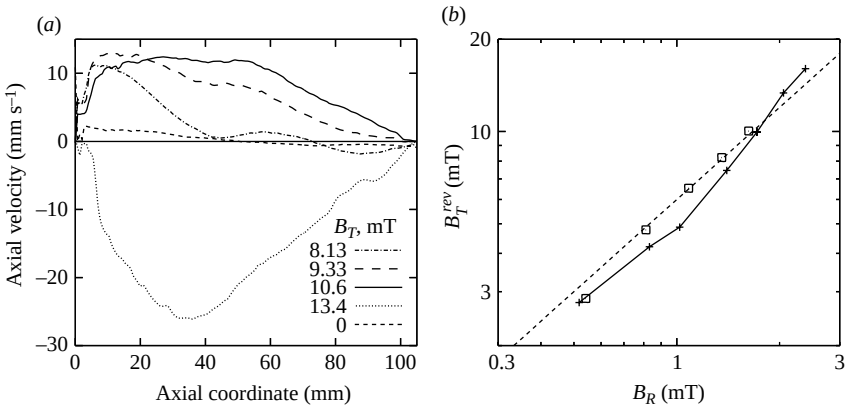

Figure 7. Axial profiles of average axial velocity at the centre of the cylinder for $B_R = 1.72$ mT (*a*); conditions of maximum upward velocity (solid line) and swirl maximum at $2d = 30$ mm (open boxes) (b). The dashed line corresponds here to equation $F = 57\mathrm{Ta}$ (cf. figure 5b).

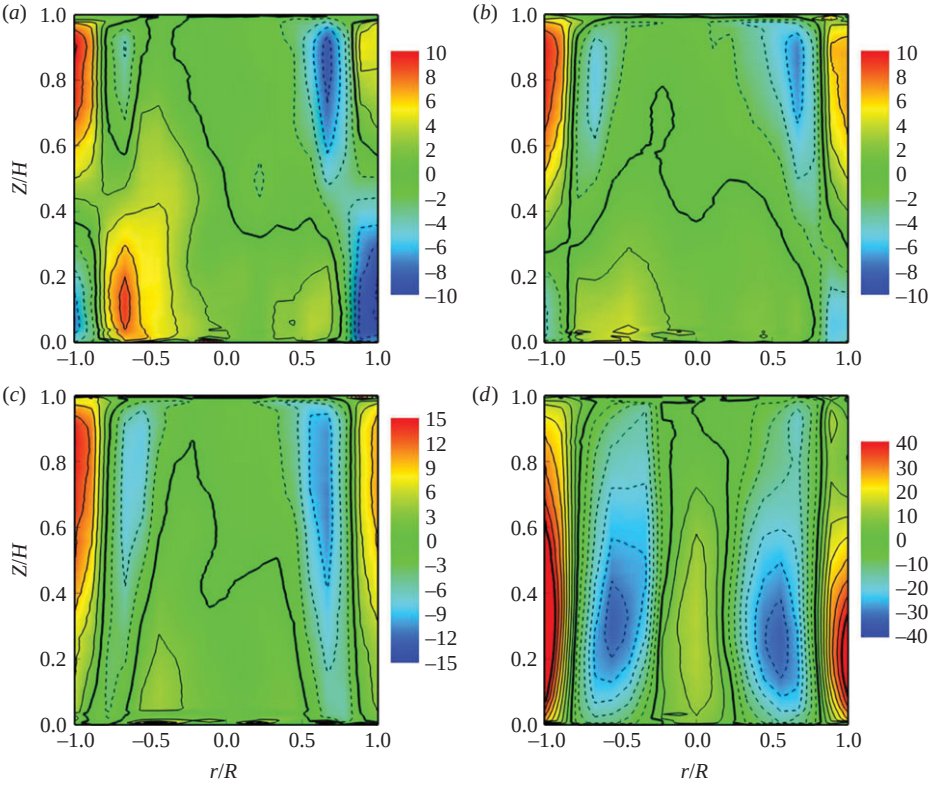

Figure 8. The mean axial velocity distributions (mm s^{-1}) in axial cross-section at $B_R = 1.72$ mT and $F/\mathrm{Ta} = 0, 5, 12, 60$ in (a–d), respectively. The isoline step is 2 or 5 mm s^{-1} in (a–c) and (d), respectively; negative isolines are dashed, the zero isoline is bold.

observed at the position $r = R/3$ ($2d = 30$ mm). The average axial velocity changed rapidly the direction to the 'normal' one as the TMF intensity was further increased.

Figure 8 shows the change of the axial velocity distribution as the TMF strength is increased. The magnitude of axial velocity did not change considerably in the

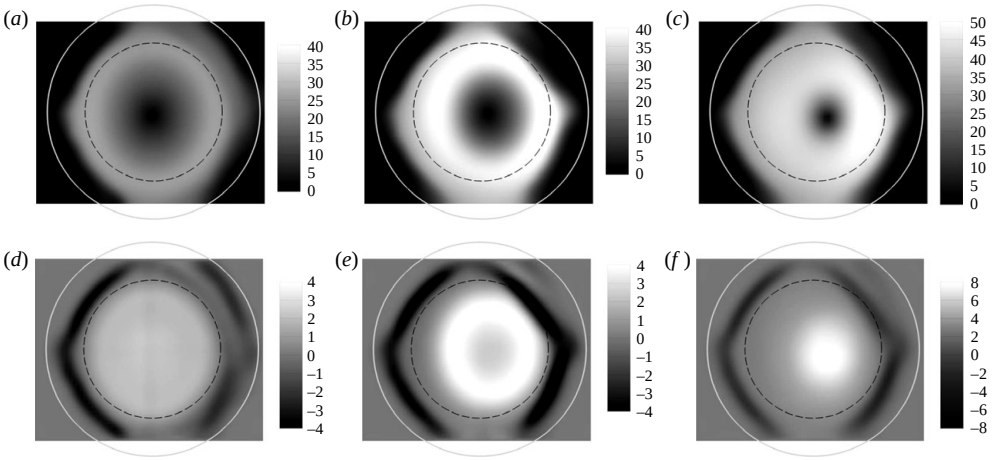

Figure 9. Average distributions of velocity magnitude in mm s^{-1} (a–c) and axial vorticity in s^{-1} (d–f) in three regimes with $B_R = 0.68$ mT: pure RMF flow (a, d); axial velocity reversal at $F/\mathrm{Ta} = 45$ (b, e); swirl concentration at $F/\mathrm{Ta} = 140$ (c, f). The outer circle displays the position of the container wall. The results may contain artefacts outside the inner dashed ring.

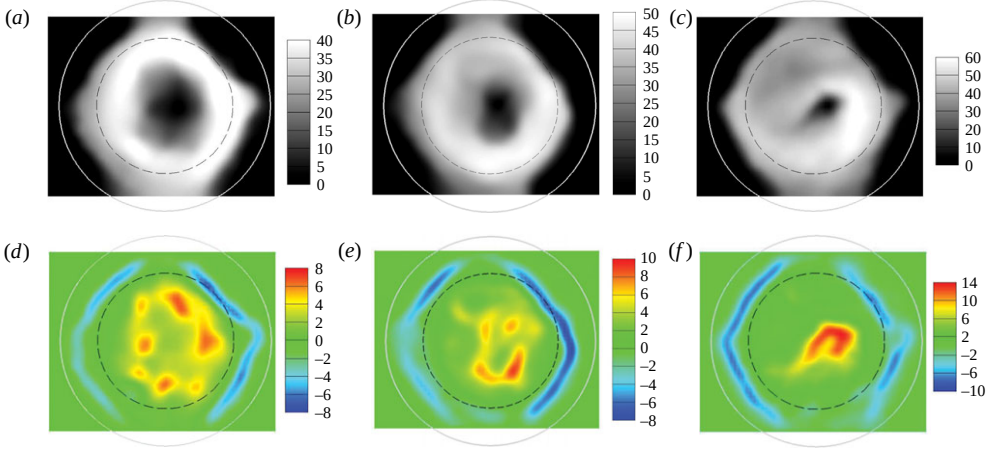

Figure 10. Characteristic snapshots of velocity magnitude in mm s^{-1} (a–c) and axial vorticity in s^{-1} (d–f) for $B_R = 0.68$ mT and $F/\mathrm{Ta} = 45$ (a, d); 70 (b, e); 140 (c, f).

RMF-dominated regime (figure 8a–c). Still, the flow pattern changed – the upper torus gradually expanded at the expense of the lower one. The regime of axial velocity reversal is depicted in figure 8(d). At a yet stronger TMF the average axial velocity at the axis turned to the 'normal' downward direction.

4.2. Surface velocity measurements

The bulk velocity measurements have revealed two distinct stages in the transition between RMF- and TMF-governed flow: the axial flow reversal at $F/\mathrm{Ta} \approx 57$ and the maximum average swirl concentration at $F/\mathrm{Ta} \approx 100$. The surface velocity measurements were focused on the di erences between these two transitional regimes. Even small surface deformations have caused reflection-induced artefacts. To avoid them we made our measurements at low velocities exclusively.

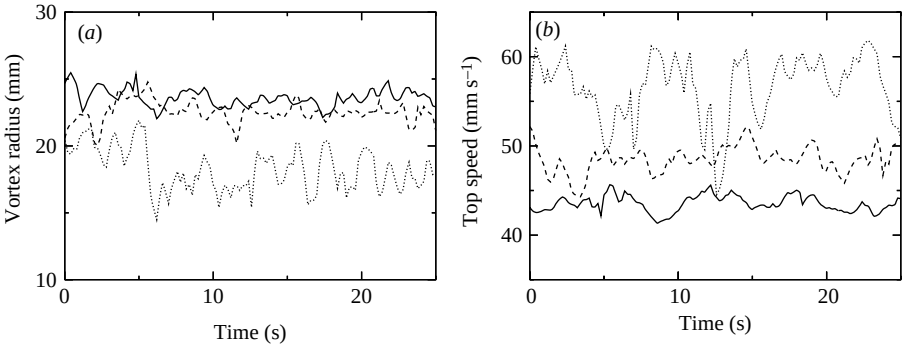

Figure 11. Time dependency of vortex radius (a) and top velocity magnitude (b) for three regimes with $B_R = 0.68$ mT and $F/\mathrm{Ta} = 45$ (solid lines); 70 (dashed lines); 140 (dotted lines).

The average velocity magnitude and axial vorticity distributions are shown in figure 9. The axial vorticity is almost constant in the core of the RMF-alone-driven flow (figure 9a, d). The regime with a vorticity ring in figure 9(b, e) corresponds approximately to the axial velocity reversal. The rotation is little influenced by the TMF at the centre. The vortex is slightly shifted from its position at $B_T = 0$. The average vorticity concentrates in a spot of about 15 mm in diameter as the poloidal forcing is increased (figure 9c, f). The average vorticity magnitude is about four times the initial value at $B_T = 0$. The spot is further shifted away from the centre of the cylinder. Both the average surface velocity and the average axial vorticity reached their maximum in this regime. An even higher poloidal forcing reduced the average velocity and vorticity. The vorticity spot lost its roundness and was further displaced. We attribute the gradual loss of symmetry to the remaining asymmetry of the TMF. As the instant vortex strengthens, the small intrinsic asymmetry is probably amplified by vortex interaction with the sidewall.

Figure 10 shows characteristic snapshots of surface velocity magnitude and vorticity fields. The 'vorticity ring' regime (figure 10a, d) is characterized by a relatively stable ring configuration with several rotating vorticity maxima. The ring diameter shrinks when the TMF is increased (figure 10b, e) and, simultaneously, the vortex centre becomes more mobile. The regime of swirl concentration (figure 10c, f) is characterized by one dominant vorticity patch of typical intensity about twice the average value. The centre of the dominant vortex moves within a circle of about 15 mm in diameter. The velocity distribution occasionally forms spiral bands. The TMF-dominated regime at yet higher B_T is more intermittent and has higher instant maximum velocities. The central vortex is volatile, more irregular and more mobile (observed within a circle of about 25 mm in diameter). Thus, the decline of average velocities in the TMF-dominated regime (figure 5a) is caused by larger excursions of the vortex and a more intermittent behaviour rather than a decline of the instant velocities.

Figure 11 shows the instant 'top speed' (defined as the average of the 110 highest nodal values of the velocity magnitude out of a total 1222 within a 60-mm-diameter ring in the central part of the frame) as well as the vortex radius. The latter is defined as average distance from those top speed nodes to the vortex centre at

$$\boldsymbol{x}_o = \frac{\sum w_i \boldsymbol{x}_i}{\sum w_i},$$

where w_i is the axial vorticity at the ith measurement point with coordinate $\boldsymbol{x}_i$. The summations are done over $w_i > 0$, and to exclude possible edge artefacts $|\boldsymbol{x}_i| < D/3$.

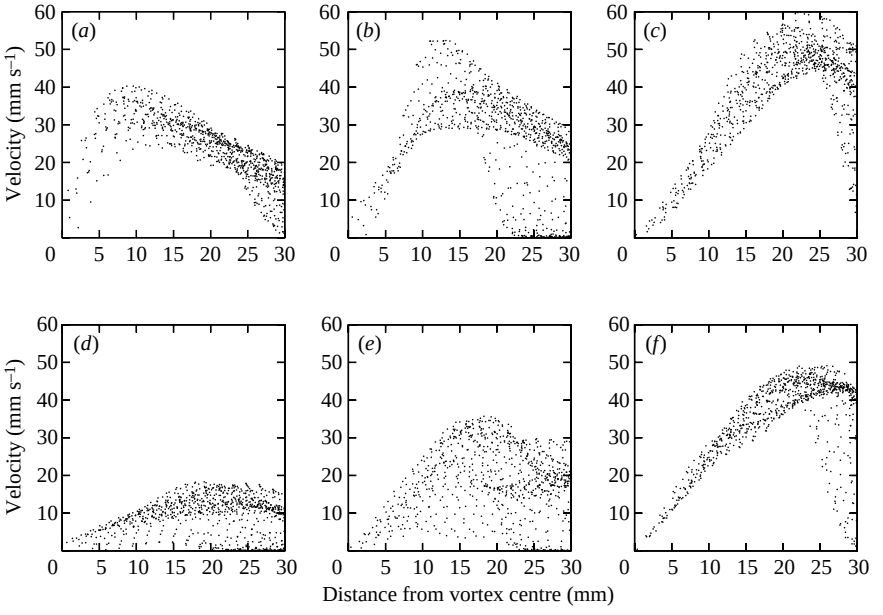

Figure 12. The instant surface velocity magnitude distributions with respect to the vortex centre at flow maximum (a–c) and minimum (d–f) for constant B_T = 5.43 mT and variable F/Ta: 275 (a, d); 160 (b, e); 70 (c, f).

The top speed represents a characteristic value of the maximum velocity magnitude on the surface. This is a certain analogue of the maximum sustained wind speed in a storm while the vortex radius defined earlier is an analogue of the maximum wind radius. The figure illustrates a decrease of the vortex radius and an increase of the top speed with increasing F at a constant azimuthal forcing Ta. This behaviour conforms with properties of the tornado simulation by Church et al. (1979) who found the far-field circulation determining the vortex radius but not influencing its top speed. Figure 12 provides additional evidence in this respect. This figure compares flow patterns of extremes (with maximum and minimum top speeds of the sequence) at a constant poloidal forcing F and variable Ta in di erent regimes. Although the azimuthal forcing varies by a factor of 4 the maximum top speed remains little influenced.

The PIV measurements were feasible only at low velocities due to surface deformations causing uncontrolled reflections and subsequent loss of contrast. However, flow visualization was possible at higher velocities using streaks of floating tracers in longer (1/50 s) exposure photographs. Figure 13 shows streak lines obtained in this way for a constant RMF and two values of TMF. The vorticity ring regime at $F/Ta \approx 70$ (figure 13a) is marked by the formation of a circular gradient zone with a diameter of around $D/2$. This gradient zone encircles a relatively quiet core. Further increase of the TMF (figure 13b) leads apparently to higher velocities and a much more compact swirl. All these observations are in a qualitative agreement with the PIV results at lower velocities.

5. *Discussion*

Concerning the controversy about the swirl in the point electrode flow, our experiment confirms the considerations of Davidson et al. (1999) that the flow may be dominated by the azimuthal body force even when the poloidal one is much larger.

(*a*)

(*b*)

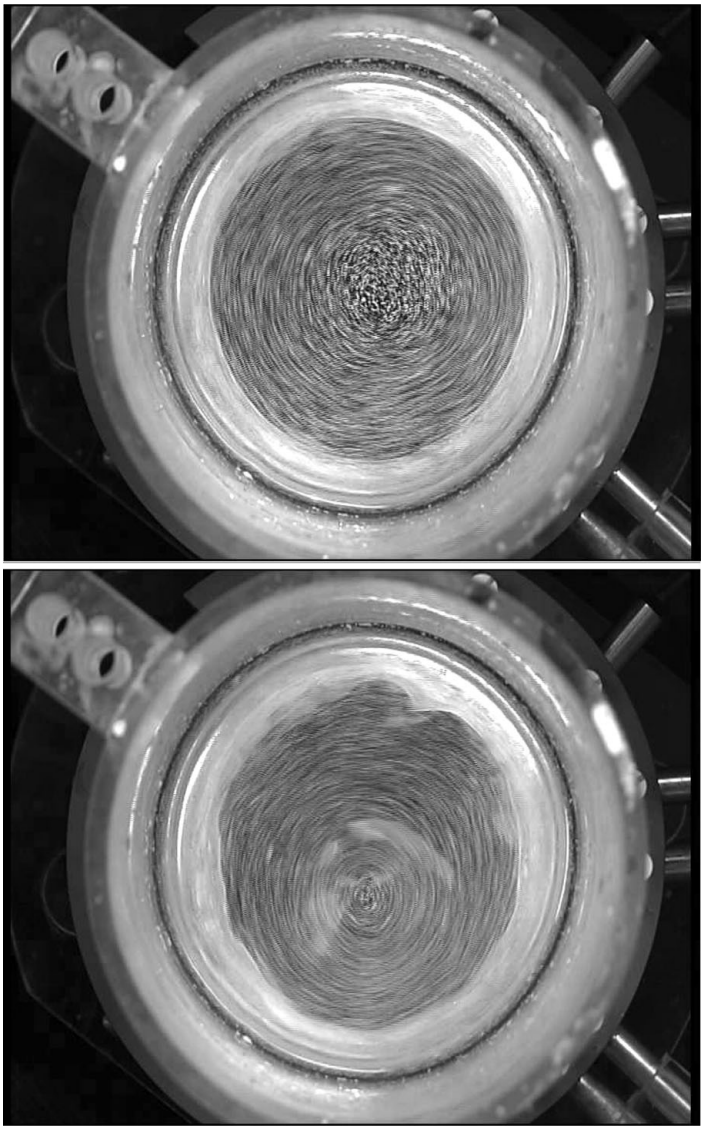

Figure 13. Streak lines of surface velocity at $B_R = 1.35$ mT in two regimes: vorticity ring $B_T = 9$ mT, $F/\mathrm{Ta} = 70$ (a); swirl concentration $B_T = 14.5$ mT, $F/\mathrm{Ta} = 180$ (b).

This fact alone, however, does not mean that it indeed happened in the point electrode experiments. The force ratio may also have been just so small that the concentrated vortex occurred. Note that a concentrated vortex solution is recognizable in the numerical results of Davidson et al. (1999) in figure 6(b). This solution shares the key features of the point electrode flow simulation results in a finite volume (Bojarevics et al. 1989, § 3.7): (i) enhancement of the azimuthal velocity towards the centre of the pool; (ii) large axial gradient of the bulk azimuthal velocity. The latter property can considerably influence the appearance of the surface depending on the direction of the electric current. Upon reversal of the current, the concentrated vortex may have been forming at the bottom of the pool and almost vanishing at the surface. In

the regime of 'poloidal suppression' (or forced uniform vortex) the core must rotate as a whole independently of the current direction while the surface radial velocity should be suppressed. Thus, the appearance of the surface should not depend on the direction of current injection. The experiment clearly shows that the current direction considerably influences the surface appearance (Bojarevics & Scherbinin 1983). Thus, the evidence is in favour of the concentrated vortex rather than a uniform one. The latter cannot, of course, be excluded in the related industrial processes. Finally, this is just a question of the force ratio.

The concentrated vortex of a spot- or ring-like structure (figure 9*e*, *f*) in our experiment is formed by interaction of a converging flow and background circulation. Intense atmospheric vortices like tornados or tropical cyclones focus their power in essentially the same way. Thus, we observed the following several similarities between them and the vortices in our experiment:

(i) the vortex structure is determined by the relative strength of the angular momentum source;

(ii) the maximum swirl velocity is determined mostly by the poloidal forcing;

(iii) the axial velocity reverses in the inner core of a wide ring-like vortex;

(iv) the vorticity ring arrangement usually breaks up into separate vortices.

It is worth exploring these similarities in more detail, since they establish a connection to a well-studied phenomenon including the extreme parameter range of tropical cyclones. Considering the persistence of these properties with respect to vastly di erent scales, driving force configurations and aspect ratios, one may expect them whenever a converging flow meets an appropriate amount of far-field angular momentum.

The poloidal and azimuthal magnetic body forces in our experiment correspond to the radial pressure drop and the far-field angular momentum driving the atmospheric vortices, respectively. Their maximum speed is mostly determined by the radial pressure drop (which, in turn, is some function of thermodynamical conditions of the environment), while the vortex structure is governed by the relative strength of the far-field angular momentum. The link between the radial pressure drop and the maximum wind speed is well known in tropical cyclones (quantitative evidence can be found, for instance, in Croxford & Barnes 2002). The velocity measurements by Church et al. (1979) in a tornado simulator also show that the swirl maximum remains constant at a fixed updraft flow rate while the far-field circulation determines the radius of the maximum speed (see Church et al. 1979, figures 14 and 17). The role of the far-field angular momentum is best evidenced in laboratory models of a tornado (Ward 1972; Church et al. 1979). These experiments show that the vortex structure or shape of the characteristic velocity distribution is controlled by the swirl ratio

$$S = \frac{\Gamma r_o}{2Q},$$

where Γ is the far-field circulation, r_o is the radius of the updraft and Q its flow rate. For a smaller S a more slender vortex is observed. Both these properties are simultaneously reflected by the following observation in tropical cyclones. Willoughby (1990) reports:

> More than 900 radial profiles of in situ aircraft observations collected in 19 Atlantic hurricanes and tropical storms over 13 years confirm that the usual mechanism of tropical cyclone intensification involves contracting maxima of the axisymmetric swirling flow.

Thus, the increase of radial pressure drop (poloidal forcing) is accompanied by a contracting vortex core and rising wind speed. Essentially the same is observed in our experiment (see figure 13).

A certain analogue of S is the Ta/F ratio in our experiment. The latter is expressed in terms of the involved forces rather than the velocity components. Figures 5(b) and 7(b) show that the following structural changes happen as this ratio reaches two thresholds. At a value of $\mathrm{Ta}/F \approx 0.01$ the maximum of average azimuthal velocity is observed in the centre of the cylinder. This regime is marked by a spot-like vorticity distribution (figures 9f and 13b). At a value of $\mathrm{Ta}/F \approx 0.02$ a reversal of the core axial velocity is found. The vorticity distribution forms a wide ring around a relatively calm uniformly rotating inner core in this regime (figures 9e and 13a). The onset of the RMF-dominated regime with a forced uniform vortex (or 'poloidal suppression') can be treated as a transition to yet another structure with the inner core occupying the entire volume.

The role of poloidal forcing in determining the top speed is demonstrated in figure 12(a–c). The azimuthal force is changed here by a factor of 4 while the corresponding velocity magnitude varies by a mere 40 %. This is probably an estimate from above since the present implementation of PIV tends to underestimate the velocity in the strongly oscillating TMF-dominated regime. We are actually observing the acid layer which, although thin, needs time to catch up with the melt motion. Besides, the instant vortex core is smaller in this regime and therefore it is more a ected by PIV filters. Note that the di erence of top speed is about just 15 % between the cases in figure 12(b, c) although the azimuthal force di ers by a factor of 2. The fluctuation amplitude increases considerably in the TMF-dominated regime. The concentrated vortex may then be temporarily suppressed by the background turbulence as illustrated in figure 12(d).

A somewhat unexpected but, in the context of atmospheric vortices, well-known feature is the reversal of the axial velocity in the vortex core or the formation of a two-cell structure (figures 7a and 8d). The axial velocity in combined RMF and TMF of di erent frequencies has been previously measured by Cramer et al. (2007) but no such phenomenon was reported since their measurements were made only outside the central part. Nolan & Farrell (1999) discuss the central subsidence in tornados with reference to vortex breakdown. There is no vortex breakdown or it occurs high above the ground when the swirl ratio S is small. As S is increased the breakdown lowers until it touches the ground forming a 'drowned vortex jump'. At a still higher S the inner core widens forming two distinct radially separated cells. All these forms may be observed in tornados (Lugt 1989) while only the two-cell regime is common in tropical cyclones with a developed eye. Although the two-cell regime is not considered as vortex breakdown (Lugt 1989), its cause appears to be the same – the centrifugal force, which limits the vortex accumulation to a certain equilibrium radius (for the physical mechanism of vortex breakdown we refer to Brown & Lopez 1990 and Gelfgat, Bar-Yoseph & Solan 1996). Vortex breakdown is associated with negative azimuthal vorticity. Its source is the axial variation of swirl in the bulk. It is observed in our experiment (figure 6a, c) for the vorticity ring regime. This is in remarkable contrast to the RMF-dominated regime shown in the same figure when the core rotates as a whole.

There is one more feature showing a certain similarity to tropical cyclones or large wedge-shaped tornados – the occurrence of multiple vortices near the radius of the maximum wind speed. These vortices are believed to form due to a Kelvin–Helmholtz instability in the free shear layer (see Montgomery et al. 2002 and references therein).

Similar multiple vortices are also observed in laboratory tornado models (Ward 1972; Church et al. 1979). Such vortices, although less pronounced, are also seen in our experiments (see figure 10*d*, *e*).

An important advantage of the magnetic flow driving is the direct and separate control of both involved body forces. This gives an opportunity to characterize the conditions of swirl accumulation in terms of the flow-driving forces instead of the observed velocities. The low Ta/F ratio supporting the tornado-like vortex shows the azimuthal force as a lever. Namely, a major change of the vortex structure is caused by an azimuthal force which is just a small fraction of the primary poloidal one. Thus, the radius of the maximum speed (area of maximum tornado damage) can be reduced by a comparably weak external azimuthal forcing. An appropriate azimuthal forcing may even detach the tornado funnel from the ground. The implementation of such a 'lever' to a real tornado is probably beyond technical capabilities of the near future. Still, this option might be worth further consideration since the 'lever ratio' in a laterally unbounded tornado may be even more favourable than in our experiment where part of the injected angular momentum is immediately lost on the sidewall.

Exploiting the discussed common properties of the concentrated vortex in a converging flow one may anticipate that the two-cell structure and vortex breakdown should also be observable in the bathtub sink flow. The small radius of the drainhole in the experiment by Andersen et al. (2006) apparently provides so strong a strain that the Burgers-vortex-type core always holds together. The larger the drainhole radius the weaker the strain rate in the core (at a fixed flow rate). At a certain threshold it should become dominated by the centrifugal force resulting in a vortex breakdown or formation of a two-cell structure. The latter indeed occurs above a wide drainhole (Montgomery et al. 2002). It seems, however, that the radius of the inner core may be imposed by the drainhole itself in the latter experiment (cf. regime with $S > 1$ in Church et al. 1979). The whole spectacular family of tornado-related phenomena (vortex breakdown, two-cell vortex and ring of multiple vortices) should emerge when the setup of Andersen et al. (2006) is equipped with an areal suction instead of a thin drainhole at the bottom. Indeed, this would then be similar to an upside-down water-filled Ward tornado simulator.

This work was supported by Deutsche Forschungsgemeinschaft in frame of the Collaborative Research Centre SFB 609. The authors appreciate the assistance of Thomas Gundrum regarding the magnetic systems and discussions with Tom Weier concerning PIV measurements. We acknowledge fruitful discussions with Jānis Priede.

REFERENCES

Andersen, A., Bohr, T., Stenum, B., Juul Rasmussen, J. & Lautrup, B. 2006 The bathtub vortex in a rotating container. J. Fluid Mech. **556**, 121–146.

Bojarevičs, V., Freibergs J., Shilova, E. I. & Scherbinin, E. V. 1989 Electrically Induced Vortical Flows. Kluwer.

Bojarevičs, V. & Scherbinin, E. V. 1983 Azimuthal rotation in the axisymmetric meridional flow due to an electric-current source. J. Fluid Mech. **126**, 413–430.

Brown, G. L. & Lopez, J. M. 1990 Axisymmetric vortex breakdown Part 2. Physical mechanisms. J. Fluid Mech. **221**, 553–576.

Church, C. R., Snow, J. T., Baker, G. L. & Agee, E. M. 1979 Characteristics of tornado-like vortices as a function of swirl ratio: a laboratory investigation. J. Atmos. Sci. **36**, 1755–1776.

Cramer, A., Pal, J. & Gerbeth, G. 2007 Experimental investigation of a flow driven by a combination of a rotating and a traveling magnetic field. Phys. Fluids **19**, 118109.

Cramer, A., Zhang, C. & Eckert, S. 2004 Local structures in liquid metals measured by ultrasonic Doppler velocimetry. Flow Meas. Instrum. **15**, 145–153.

Croxford, M. & Barnes, G. M. 2002 Inner core strength of Atlantic tropical cyclones. Mont. Weather Rev. **130**, 127–139.

Davidson, P. A. 1992 Swirling flow in an axisymmetric cavity of arbitrary profile, driven by a rotating magnetic field. J. Fluid Mech. **245**, 669–699.

Davidson, P. A. 2001 An Introduction to Magnetohydrodynamics. Cambridge University Press.

Davidson, P. A., Kinnear, D., Lingwood, R. J., Short, D. J. & He, X. 1999 The role of Ekman pumping and the dominance of swirl in confined flows driven by Lorentz forces. Eur. J. Mech. B/Fluids **18**, 693–711.

Emanuel, K. A. 1991 The theory of hurricanes. Annu. Rev. Fluid Mech. **23**, 179–196.

Emanuel, K. A. 2003 Tropical cyclones. Annu. Rev. Earth Planet. Sci. **31**, 75–104.

Gelfgat, A. Yu., Bar-Yoseph, P. Z. & Solan, A. 1996 Stability of confined swirling flow with or without vortex breakdown. J. Fluid Mech. **311**, 1–36.

Gelfgat, Yu., Krūmiņš, J. & Abricka, M. 1999 Motion of an electrically conducting fluid in a cylindrical volume exposed to the influence of superimposed rotating and travelling magnetic fields. Magnitnaya Gidrodinamika **36**, 3–16 (in Russian).

Gelfgat, Yu., Skopis, M. & Grabis, J. 2005 Electromagnetically driven vortex flow to introduce small solid particles into liquid metal. Magnetohydrodynamics **41**, 249–254.

Gorbachev, L. P., Nikitin, N. V. & Ustinov A. L. 1974 Magnetohydrodynamic rotation of an electrically conductive liquid in a cylindrical vessel of finite dimensions. Magnitnaya Gidrodinamika **10**, 406–414 (in Russian).

Grants, I. & Gerbeth, G. 2004 Stability of melt flow due to a traveling magnetic field in a closed ampoule. J. Cryst. Growth **269**, 630–638.

Klemp, J. B. 1987 Dynamics of tornadic thunderstorms. Annu. Rev. Fluid Mech. **19**, 369–402.

Lantzsch, R., Galindo, V., Grants, I., Zhang, C., Pätzold, O., Gerbeth, G. & Stelter, M. 2007 Experimental and numerical results on the fluid flow driven by a traveling magnetic field. J. Cryst. Growth **305**, 249–256.

Lugt, H. J. 1989 Vortex breakdown in atmospheric columnar vortices. Bull. Am. Met. Soc. **70**, 1526–1537.

Maxworthy, T. 1973 A vorticity source for large-scale dust devils and other comments on naturally occuring columnar vortices. J. Atmos. Sci. **30**, 1717–1722.

Montgomery, M. T., Vladimirov, V. A & Denissenko, P. V. 2002 An experimental study on hurricane mesovortices. J. Fluid Mech. **471**, 1–32.

Nolan, D. S. & Farrell, B. F. 1999 The structure and dynamics of tornado-like vortices. J. Atmos. Sci. **56**, 2908–2936.

Shapiro, A. H. 1962 Bath-tub vortex. Nature **196**, 1080–1081.

Sozou, C. & Pickering, W. M. 1976 Magnetohydrodynamic flow due to the discharge of an electric current in a hemispherical container. J. Fluid Mech. **73**, 641–650.

Stiller, J., Koal, K., Fraňa, K. & Grundmann, R. 2006 Stirring of melts using rotating and travelling magnetic fields. In Proc. 5th Intl Conf. on CFD in the Process Industries, Melbourne, Australia (ed. P. J. Witt & M. P. Schwarz). CSIRO, Collingwood.

Takeda, Y. 1991 Development of an ultrasound velocity profile monitor. Nucl. Engng Des. **126**, 277–284.

Ward, N. B. 1972 The exploration of certain features of tornado dynamics using a laboratory model. J. Atmos. Sci. **29**, 1194–1204.

Willoughby, H. E. 1990 Temporal changes of the primary circulation in tropical cyclones. J. Atmos. Sci. **47**, 242–264.